
Conditional Sampling With Monotone GANs

Nikola B. Kovachki

Computing and Mathematical Sciences
California Institute of Technology
Pasadena, CA 91125
nkovachki@caltech.edu

Ricardo Baptista

Aeronautics and Astronautics
Massachusetts Institute of Technology
Cambridge, MA 02139
rsb@mit.edu

Bamdad Hosseini

Computing and Mathematical Sciences
California Institute of Technology
Pasadena, CA 91125
bamdadh@caltech.edu

Youssef Marzouk

Aeronautics and Astronautics
Massachusetts Institute of Technology
Cambridge, MA 02139
ymarz@mit.edu

Abstract

We present a new approach for sampling conditional measures that enables uncertainty quantification in supervised learning tasks. We construct a mapping that transforms a reference measure to the probability measure of the output conditioned on new inputs. The mapping is trained via a modification of generative adversarial networks (GANs), called monotone GANs, that imposes monotonicity constraints and a block triangular structure. We present theoretical results, in an idealized setting, that support our proposed method as well as numerical experiments demonstrating the ability of our method to sample the correct conditional measures in applications ranging from inverse problems to image in-painting.

1 Introduction

Consider inputs $\mathbf{x} \in \mathbb{R}^n$ and outputs $\mathbf{y} \in \mathbb{R}^m$ distributed according to a joint probability measure $\nu(d\mathbf{x}, d\mathbf{y})$. We introduce a method called *monotone generative adversarial networks* (MGANs) to approximately sample the conditional measure $\nu(d\mathbf{y}|\mathbf{x}^*)$ given any new input $\mathbf{x}^* \in \mathbb{R}^n$, by constructing a map $F(\mathbf{x}^*, \cdot)$ that pushes forward a reference measure $\eta(d\mathbf{y})$ to $\nu(d\mathbf{y}|\mathbf{x}^*)$.

Conditional sampling is a fundamental task for machine learning and statistics, and in particular for supervised learning (SL), as it provides a way of quantifying uncertainty in the predicted outputs (see Section A). Standard SL algorithms assume a model of the form $\mathbf{y} = G(\mathbf{x})$, with \mathbf{x} regarded as a random variable and G a possibly stochastic mapping accounting for output noise. Deterministic SL algorithms such as ridge, LASSO, or neural network regression [20] approximate G with a deterministic map \hat{G} within a parameterized function space. Probabilistic methods such as Bayesian techniques improve upon this approach by modeling \hat{G} as a random function, parametrically or nonparametrically; a prior measure on \hat{G} is combined with a likelihood function to identify a posterior measure on \hat{G} . To this end, Bayesian methods approximate the law of $\mathbf{y}|\mathbf{x}^*$ with the law of $\hat{G}(\mathbf{x}^*)$. Both deterministic and Bayesian approaches to SL rely on prior information about G , such as its parameterization or the nature of the stochasticity in $\mathbf{y}|\mathbf{x}^*$. However, these prior assumptions are often impossible to verify in practice, and hence model selection techniques [20, Ch. 8] are often employed to choose the “best” model for G from within a large class.

In contrast, recent unsupervised learning methods such as generative adversarial networks (GANs) [15, 32, 3, 18], normalizing flows (NFs) [27, 34], and variational autoencoders (VAEs) [9] have been

remarkably successful at sampling complex and high dimensional probability distributions under minimal assumptions on the underlying models for the data. Put simply, these generative methods train a map T that pushes forward a reference measure η to the target distribution $\nu(d\mathbf{x}, d\mathbf{y})$. (In some cases, such as VAEs and GANs, the measure η is usually supported on a lower dimensional space than ν .) The map T is often parameterized with a neural network and is trained only using a dataset consisting of samples from $\nu(d\mathbf{x}, d\mathbf{y})$, and without any explicit assumptions on the relationship between \mathbf{y} and \mathbf{x} . Generative models are typically not designed with conditional sampling in mind, however, and to our knowledge, it is not possible to utilize the map T constructed by GANs or VAEs to directly sample the conditionals $\nu(d\mathbf{y}|\mathbf{x}^*)$. We note that the conditional sampling problem of interest to our work is inherently different from that considered in conditional GANs [31], where ν is taken to be a multi-modal measure and a GAN is trained to generate samples from different modes of ν once the label of the desired mode is specified. The same approach is not applicable in our setting because for each \mathbf{x}_i in the training set, we often have only a single sample $\mathbf{y}_i|\mathbf{x}_i$. On the other hand, invertible NFs [8, 35, 26, 25] could, with some care, be re-purposed to perform conditional sampling by use of Theorem 1 below. However these methods require specialized architectures and training procedures without offering clear advantages over the GAN framework. In the GAN setting, some recent work (e.g., [49, 22]) employs modifications of GANs to solve image-to-image translation problems, which fall within the class of SL problems. However these approaches are very specific to imaging and do not guarantee that the constructions obtain the correct conditionals for general measures $\nu(d\mathbf{x}, d\mathbf{y})$. While this issue may not be of concern in imaging with regard to photorealism, it is essential in SL if one is to have any confidence in uncertainty estimates. Another relevant body of work focuses on conditional density estimation using mixture models that are parameterized with neural networks [6, 41], or more flexible nonparametric models [2, 43, 1]. However, parametric methods impose structural constraints on the target conditional densities and do not focus on conditional *sampling* as we do here, while nonparametric methods typically have growing sampling costs with the size of the dataset and require careful regularization to avoid overfitting.

Here we propose a method that bridges the gap between SL and generative modeling. We train a map T without any model assumptions between \mathbf{y} and \mathbf{x} —i.e., we do not assume a G —but we enforce sufficient constraints that allow us to extract another map F from T so that $F(\mathbf{x}^*, \cdot)$ can be used for sampling $\nu(d\mathbf{y}|\mathbf{x}^*)$. This idea has been explored in the uncertainty quantification (UQ) and inverse problems communities [30, 10, 5, 38, 44] for Bayesian inference, by constructing monotone triangular maps T that approximate the well-known triangular Knothe–Rosenblatt (KR) map [42, Sec. 2.3]. By construction, the components of the KR map push forward the reference conditionals to the target conditionals, which is precisely what is desired for conditional sampling tasks. Working with the KR map, however, can be restrictive in terms of its parameterization since we must ensure the map is triangular and monotone. Thus, we relax the triangular assumption to a block triangular assumption and show that this relaxed constraint is sufficient for conditional sampling. We then impose the block triangular structure of T and strict monotonicity as constraints in the GAN framework to train a map T from which the desired map F can be extracted easily; hence the name MGAN.

Proofs, discussions, and additional results and details pertaining to numerical experiments are available in the appendix.

2 Block triangular transformations of measures

We now outline our approach to the construction of block triangular maps for conditional sampling. Following the notation of Section 1, we consider input and output pairs $\mathbf{x} \in \mathbb{R}^n$ and $\mathbf{y} \in \mathbb{R}^m$ and define their concatenation $\mathbf{z} := (\mathbf{x}, \mathbf{y}) \in \mathbb{R}^d$ with $d = n + m$. We then consider the measure transport problem [46] of pushing a *reference measure* $\eta(d\mathbf{z}) \equiv \eta(d\mathbf{x}, d\mathbf{y})$ to the joint *target measure* $\nu(d\mathbf{z}) \equiv \nu(d\mathbf{x}, d\mathbf{y})$ by finding a map $T : \mathbb{R}^d \rightarrow \mathbb{R}^d$ so that $T_\# \eta = \nu$. The existence of such a map can be guaranteed under very general conditions, for example by assuming that η, ν have no atoms.

From the GAN perspective, T would be the *generator* map, but our construction already differs from standard GAN generators that often map low dimensional reference measures to high dimensional output (image space) measures. The existence of a transport map cannot be guaranteed in that case unless $\nu(d\mathbf{x}, d\mathbf{y})$ is supported on a low-dimensional manifold embedded in \mathbb{R}^d whose intrinsic dimension is at most the dimension of the latent space (see Section D for a simple example). Hence, we do not make the manifold assumption for two reasons: 1) it does not hold for many SL problems

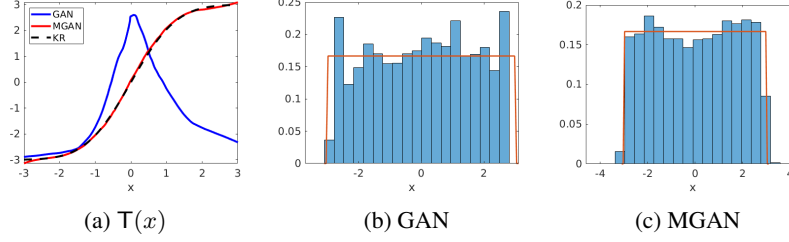


Figure 1: Comparison between GANs and MGANs for pushing $N(0, 1)$ to $U(-3, 3)$. (a) The map T obtained from GANs, MGANs, and the analytically computed KR map demonstrating that the KR and MGAN maps are invertible while the GAN map is not. (b, c) Histogram of GAN and MGAN pushforward samples demonstrating that both methods approximate the uniform distribution $U(-3, 3)$ with acceptable quality.

such as inverse problems in scientific applications, and 2) it is unclear how to define notions of monotonicity and invertibility without any knowledge of the manifold geometry.

We require the map T to be of *block triangular* form, that is,

$$T(x, y) = \begin{bmatrix} K(x) \\ \tilde{F}(x, y) \end{bmatrix}, \quad K : \mathbb{R}^n \rightarrow \mathbb{R}^n, \quad \tilde{F} : \mathbb{R}^d \rightarrow \mathbb{R}^m. \quad (1)$$

Furthermore, we say T is strictly monotone [48] if $\langle T(z) - T(z'), z - z' \rangle > 0$, for all $z, z' \in \mathbb{R}^d$, $z \neq z'$, with $\langle \cdot, \cdot \rangle$ denoting the Euclidean inner product, and we use $\mathcal{T}(\mathbb{R}^d)$ to denote the space of block triangular, continuous, and strictly monotone maps from \mathbb{R}^d into \mathbb{R}^d .

Remark 1. The monotonicity constraint (together with other mild conditions) ensures that T , and by extension K , are invertible which, as we discuss below, is crucial for our method. We also note that without this constraint the map T can become non-invertible as depicted in Figure 1. Here we consider the problem of pushing a standard normal distribution $N(0, 1)$ to the uniform measure $U(-3, 3)$. As demonstrated in Figure 1(a) the GAN map is not invertible while the MGAN map is monotone and hence invertible; in fact, the MGAN map approximates the KR map in this case.

To simplify our arguments, we henceforth assume that $\nu(dz)$ is absolutely continuous with respect to the Lebesgue measure on \mathbb{R}^d with full support, i.e., its Lebesgue density is strictly positive. As for $\eta(dz)$ we simply assume $\eta = N(0, I_d)$ with I_d denoting the $d \times d$ identity matrix.

Remark 2. Our assumptions on ν and η can be relaxed significantly. For example, we only need the target ν along with its marginal $\nu(d\mathbf{x})$ and conditional $\nu(d\mathbf{y}|\mathbf{x})$ to have no atoms, per the minimum requirements for existence of triangular maps between Borel measures [7, Thm. 10.10.30]. However, these stronger assumptions guarantee a continuous and invertible map T which is easier to handle analytically and numerically. Moreover, the choice of the standard Gaussian for η is innocuous and can be replaced with any product measure of the form $\eta(d\mathbf{x}, d\mathbf{y}) = \eta_1(d\mathbf{x}) \otimes \eta_2(d\mathbf{y})$.

Remark 3. For classification problems, the labels, with a one-hot encoding, fall on the extreme points of the probability simplex; hence the conditional $\nu(d\mathbf{y}|\mathbf{x})$ has atoms, and we cannot guarantee the existence of transport maps. One may relax the label definitions so that the support of $\nu(d\mathbf{y}|\mathbf{x})$ has positive Lebesgue measure $\epsilon > 0$. However, it is unclear if this approach leads to a consistent algorithm, i.e., whether the pushforward $T_{\#}\eta$ coincides with the correct conditional as $\epsilon \rightarrow 0$. Moreover, it is unclear how to interpret label uncertainties when $\epsilon > 0$ is fixed. These questions merit further analysis and constitute interesting future work that we will not undertake here.

Under the above assumptions we now formulate a measure transport optimization problem:

$$\min_T D(T_{\#}\eta|\nu) \quad \text{s.t.} \quad T \in \mathcal{T}(\mathbb{R}^d), \quad (2)$$

where D denotes an appropriate statistical divergence [29, 15], i.e., a functional that measures the difference between probability measures satisfying $D(\mu_1|\mu_2) \geq 0$ and $D(\mu_1|\mu_2) = 0$ if and only if $\mu_1 = \mu_2$. Under our assumptions the KR map is a global minimizer of Problem (2) achieving $D(T_{\#}\eta|\nu) = 0$. In fact, the KR map could be constructed explicitly if the component-wise marginals and conditionals of η and ν were known. By construction, the KR map is fully triangular, i.e., its

Jacobian is a triangular matrix [42, Sec. 2.3] and thus it satisfies stricter constraints than the block triangular constraint imposed in (2). As noted in [30, Sec. 4.1], for specific choices of D such as the Kullback–Leibler (KL) divergence and under stronger constraints, the KR map is the unique minimizer of (2). Here we sacrifice uniqueness of the minimizer in exchange for more relaxed constraints since by Theorem 1, any global minimizer of (2) is sufficient for conditional sampling.

2.1 Conditional sampling

Employing our construction (1), we obtain the following theorem which serves as the theoretical cornerstone of our conditional sampling procedure. This result states that given a global minimizer of (2), we can directly construct a mapping between the marginal reference measure $\eta(d\mathbf{y}) = N(0, I_m)$ and the target conditional $\nu(d\mathbf{y}|\mathbf{x}^*)$ by composing the component \tilde{F} with K^{-1} . The proof is given in Section C, following the same steps as the proof of [30, Lem. 1].

Theorem 1. *Let T be a global minimizer of (2), expressed in the form (1), and assume T is surjective. Then for any new input $\mathbf{x}^* \in \mathbb{R}^n$ it holds that $\tilde{F}(K^{-1}(\mathbf{x}^*), \cdot)_\# \eta(d\mathbf{y}) = \nu(d\mathbf{y}|\mathbf{x}^*)$.*

Remark 4. *The requirement that T is surjective is not very restrictive in practice. Since T is strictly monotone it follows from the Browder–Minty theorem [48, Thm. 26.A] that it is surjective provided that it is also coercive, i.e., $\lim_{\|\mathbf{x}\| \rightarrow +\infty} \frac{\langle T(\mathbf{x}), \mathbf{x} \rangle}{\|\mathbf{x}\|} = +\infty$. If coercivity cannot be verified directly we can always perturb T sufficiently far away from the training set to ensure coercivity. This also guarantees that the inverse K^{-1} is well defined.*

The conditioning procedure can be further simplified by reparameterizing T to circumvent the need for inverting K . Since K^{-1} exists we define a new map $F(\mathbf{x}, \mathbf{y}) := \tilde{F}(K^{-1}(\mathbf{x}), \mathbf{y})$ and rewrite (1) in the form

$$T(\mathbf{x}, \mathbf{y}) = \begin{bmatrix} K(\mathbf{x}) \\ F(K(\mathbf{x}), \mathbf{y}) \end{bmatrix}. \quad (3)$$

Applying Theorem 1 with F in place of \tilde{F} then yields

$$F(\mathbf{x}^*, \cdot)_\# \eta(d\mathbf{y}) = \nu(d\mathbf{y}|\mathbf{x}^*). \quad (4)$$

Note that we can also use (4) for conditional density estimation: Letting $\pi_\nu(\mathbf{y}|\mathbf{x}^*)$ and $\pi_\eta(\mathbf{y})$ denote the probability density functions of $\nu(d\mathbf{y}|\mathbf{x}^*)$ and $\eta(d\mathbf{y})$ respectively, the change of variables formula yields $\pi_\nu(\mathbf{y}|\mathbf{x}^*) = \pi_\eta \circ F^{-1}(\mathbf{x}^*, \mathbf{y}) |\det \nabla_{\mathbf{y}} F^{-1}(\mathbf{x}^*, \mathbf{y})|$, where $F^{-1}(\mathbf{x}^*, \mathbf{y})$ is the inverse of the map $\xi \mapsto F(\mathbf{x}^*, \xi)$. The map $F^{-1}(\mathbf{x}^*, \cdot)$ can be evaluated with standard root-finding methods [30] or parametrized as a neural network and trained via regression by noting that (4) allows for generating an unlimited number of training samples for this task once F is fixed. Further, note that if density estimation is the primary goal, then estimating directly the inverse map $F^{-1}(\mathbf{x}^*, \mathbf{y}) := S(\mathbf{x}^*, \mathbf{y})$ yields $\pi_\nu(\mathbf{y}|\mathbf{x}^*) = \pi_\eta \circ S(\mathbf{x}^*, \mathbf{y}) |\det \nabla_{\mathbf{y}} S(\mathbf{x}^*, \mathbf{y})|$, which eliminates the need for inverting F to characterize the conditional density. Since we are focused here on efficient conditional sampling procedures, we leave the conditional density estimation direction for future research.

2.2 The training and sampling procedures

We now outline a practical procedure for sampling the conditional $\nu(d\mathbf{y}|\mathbf{x}^*)$ based on (4), also summarized in Section B. Consider Problem (2) with the standard GAN min-max functional for D . Since the optimal discriminator gives the Jensen–Shannon divergence up to a constant, this choice is valid in (2). Indeed, as shown in [32], a variety of divergences may be tightly lower-bounded by similar min-max functionals—a more general feature of dual formulations of measure transport problems [47]. We approximate the components K and F of T with neural networks and replace the strict monotonicity constraint on T with an average monotonicity constraint. Then, assuming T is in the form (3), we have the optimization problem:

$$\min_{K, F} \max_f \mathbb{E}_{\mathbf{z} \sim \nu} [\log f(\mathbf{z})] + \mathbb{E}_{\mathbf{w} \sim \eta} [\log(1 - f(T(\mathbf{w})))] - \lambda \mathbb{E}_{\mathbf{w} \sim \eta} \mathbb{E}_{\mathbf{w}' \sim \eta} \langle T(\mathbf{w}) - T(\mathbf{w}'), \mathbf{w} - \mathbf{w}' \rangle. \quad (5)$$

Here f denotes the discriminator and $\lambda > 0$ is a Lagrange multiplier controlling the weight of the average monotonicity constraint. While this condition does not ensure that T is monotone on the support of η , numerically we find that it is sufficient to ensure that T is monotone with high probability, as demonstrated in Section E.5. Indeed, the probability that T is monotone can be easily

tracked during training to certify the invertibility of the resulting map. Furthermore, note that, in contrast to training procedures based on minimizing KL divergence, solving (5) does not require computing Jacobian determinants of T . The resulting procedure is outlined in detail in Section B.

Once the map T is trained, we proceed to generate new approximate samples from the conditional measure $\nu(d\mathbf{y}|\mathbf{x}^*)$ as follows: we generate a set of i.i.d. samples $\mathbf{u}_i \sim \eta(d\mathbf{y})$ drawn from the reference marginal and simply set $\mathbf{y}_i = F(\mathbf{x}^*, \mathbf{u}_i)$. Assuming that the components of T are good approximations to a global minimizer of (2) we expect the \mathbf{y}_i to be approximately distributed according to $\nu(d\mathbf{y}|\mathbf{x}^*)$ following (4). These new samples can then be used to compute statistics and uncertainty estimates derived from the conditional distribution of the output variable \mathbf{y} .

Remark 5. *We note that (5) constitutes the most basic form of a GAN with additional monotonicity and block-triangular constraints. Much recent effort has been dedicated to stabilizing the GAN training procedure through new cost functionals, constraints, and algorithms, and all of these ideas can be incorporated within our framework seamlessly. We choose to state and implement (5) to demonstrate the effectiveness of MGANs in their simplest form, and also for clarity of exposition.*

3 Experiments

We now present four numerical experiments that demonstrate the effectiveness of MGANs in various conditional sampling applications, ranging from inverse problems to image in-painting. In Section 3.1 we present a synthetic example demonstrating the effectiveness of MGANs for a variety of nonlinear regression problems with non-Gaussian noise models. Here we obtain accurate credible intervals for our predictions, elucidating the uncertainty quantification capabilities of our SL procedure. In Section E.2 we present a benchmark problem for sampling methods that exhibits a highly non-Gaussian posterior measure. We show that MGANs improve upon previous work [30] that utilizes a related transport map formulation. Next, in Section 3.3 we present a benchmark inverse problem in engineering that highlights MGANs' ability to capture the inverse of a complicated map involving a partial differential equation (PDE). Our final example in Section 3.4 concerns image in-painting, and demonstrates the feasibility and effectiveness of MGANs in high-dimensional problems. A complete list of neural network architectures as well as hyperparameters used in all experiments are summarized in Section E.

3.1 A synthetic example

We start with an example in two dimensions where the map T can be computed explicitly. Consider the following input-to-output maps,

$$y = \tanh(x) + \gamma, \quad \gamma \sim \Gamma(1, 0.3), \quad (6)$$

$$y = \tanh(x + \gamma), \quad \gamma \sim N(0, 0.05), \quad (7)$$

$$y = \gamma \tanh(x), \quad \gamma \sim \Gamma(1, 0.3), \quad (8)$$

where $x \sim U[-3, 3]$ in all three cases. We choose \tanh as our regression function since it is nonlinear and can be used as a continuum model for classification problems.

Figure 2 shows the trained MGAN on each of the above problems using $N = 50000$ training data points. Figure 2(a,b) demonstrate the ability of MGANs to capture the joint measures $\nu(dx, dy)$. Figure 2(c) shows the conditional means of $y|x^*$ computed analytically and by sampling $F(x^*, \cdot)_{\#}\eta(x)$. We observe that the MGAN means are a good match to the true conditional means and also that the MGAN uncertainty estimates (in this case \pm twice the sample standard deviation) are close to the analytic values. This is an example of the MGANs' ability to accurately predict $y|x^*$ and quantify uncertainty. Figure 2(d) further highlights the capabilities of MGANs by demonstrating the closeness of the MGAN sample histogram to the analytic conditional densities.

3.2 Biochemical oxygen demand model

We turn to an inference problem in biochemical oxygen demand (BOD) modeling also studied in [30, 37, 4]. Consider the time-dependent model $B(t) = A(1 - e^{-Bt}) + \gamma$, where A and B are unknown parameters and $\gamma \sim N(0, 10^{-3})$ is the observational noise. We model $A \sim U(0.4, 1.2)$ and $B \sim U(0.01, 0.31)$ as independent, uniform random variables and assume to have observations

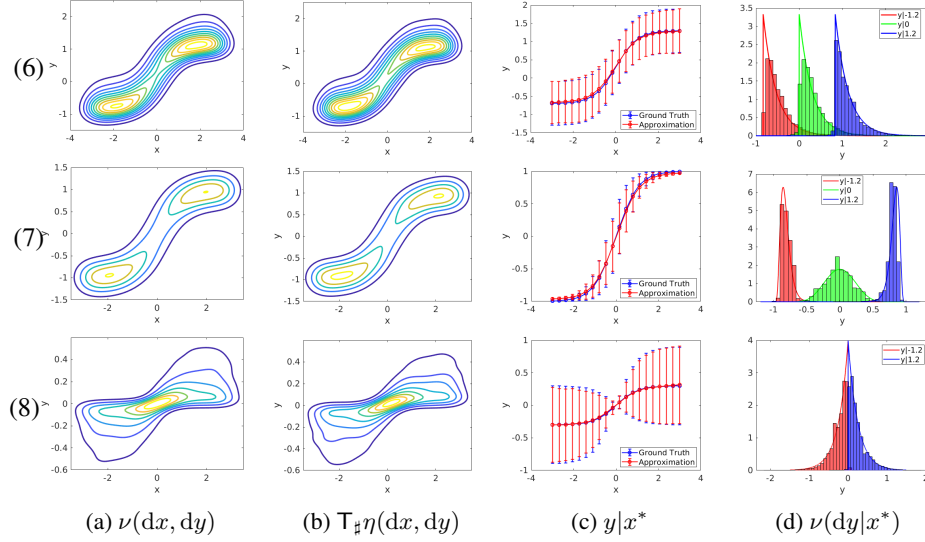


Figure 2: The rows of images correspond to problems (6), (7), (8) respectively. Column (a) shows the true joint densities $\nu(x, y)$. Column (b) shows a KDE of MGAN approximations to $\nu(x, y)$ computed using 20,000 samples from $T_{\#}\eta$. Column (c) shows the conditional mean along with error bars of twice the standard deviation of $y|x_j^*$ at $x_j^* = -3 + j(6/19)$ with $j = 0, \dots, 19$. Column (d) shows the true densities of $y|x_j^*$ as well as histograms of MGAN samples for $x_j^* = -1.2 + j1.2$ with $j = 0, 1, 2$. Note that, for (8), $y|0$ is omitted since $y|0 = \delta_0$.

of the forward map $\mathcal{B}(t)$ at times $t = 1, 2, 3, 4, 5$. Hence, given a realization of the random variables A, B , our training data is of the form $\mathbf{x} = (\mathcal{B}(1), \dots, \mathcal{B}(5))$ and $\mathbf{y} = (A, B)$. We further define the transformed parameters $\rho_1 = \sqrt{2}\text{erf}^{-1}\left(\frac{A-0.4}{0.4} - 1\right)$ and $\rho_2 = \sqrt{2}\text{erf}^{-1}\left(\frac{B-0.01}{0.15} - 1\right)$. The uniform distributions assumed for A, B then imply $\boldsymbol{\rho} = (\rho_1, \rho_2) \sim N(0, I_2)$ *a priori*. We choose to infer the $\boldsymbol{\rho}$ variables rather than the \mathbf{y} variables to directly compare our results with [30]. Since these transformations are invertible, solving for $\boldsymbol{\rho}$ is equivalent to solving for \mathbf{y} . We will solve the problem in two settings: in the *without prior* case we directly infer $\mathbf{y}|x^*$ (assuming no knowledge of the prior transformations) and afterwards convert the conditional \mathbf{y} samples to $\boldsymbol{\rho}$ samples. In the second case, which we call *with prior*, we directly sample $\boldsymbol{\rho}|x^*$.

Following [30], we sample the conditional at $\mathbf{x}^* = (\mathcal{B}(0.18), \mathcal{B}(0.32), \mathcal{B}(0.42), \mathcal{B}(0.49), \mathcal{B}(0.54))$. Table 1 shows various statistics of the conditional $\boldsymbol{\rho}|x^*$. The ground truth statistics, computed with MCMC, are taken from [30]. When training with $N = 5000$ training data points each of our models improves on at least 6 of the 8 statistics and at least 7 of the 8 statistics when $N = 50000$ compared to [30]. Figure 3 shows kernel density estimates (KDE) of $\boldsymbol{\rho}|x^*$ samples demonstrating the ability of MGANs to capture the true conditional densities.

Table 1: Statistics of $\boldsymbol{\rho}|x^*$ for the BOD problem. Bold numbers are closest to those obtained using MCMC in each column.

Map type	N	Mean		Variance		Skewness		Kurtosis	
		ρ_1	ρ_2	ρ_1	ρ_2	ρ_1	ρ_2	ρ_1	ρ_2
MCMC “truth”		0.075	0.875	0.190	0.397	1.935	0.681	8.537	3.437
[30]	5000	0.090	0.908	0.180	0.490	2.968	0.707	29.589	16.303
	50000	0.034	0.902	0.206	0.457	1.628	0.872	7.568	3.876
MGAN (without prior)	5000	0.075	0.762	0.193	0.331	1.079	0.451	3.980	3.048
	50000	0.071	0.843	0.196	0.358	2.003	0.538	7.961	3.246
MGAN (with prior)	5000	0.084	0.805	0.278	0.402	1.947	0.805	8.122	4.363
	50000	0.038	0.882	0.205	0.397	2.132	0.490	8.9747	3.408

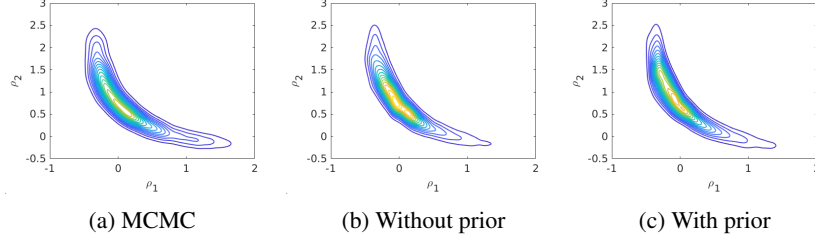


Figure 3: KDE of $\rho|\mathbf{x}^*$ samples for the BOD problem obtained from (a) 30000 MCMC samples as a benchmark and (b,c) from 30000 MGAN samples trained with $N = 50000$ training data.

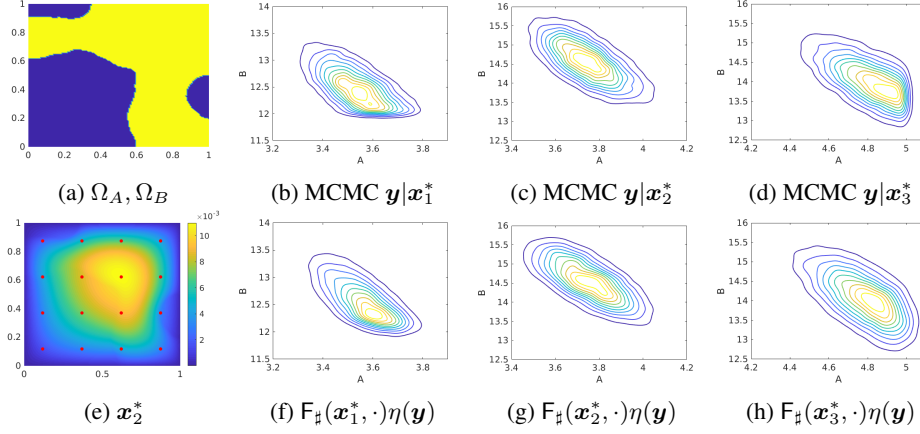


Figure 4: KDEs of the conditionals $\mathbf{y}|\mathbf{x}_j^*$ for the Darcy flow problem with $j = 1, 2, 3$, computed from 30,000 representative samples shown in the last column. The first row shows the results obtained by MCMC. The second row shows the MGAN results trained with $N = 100000$ training data points.

3.3 Darcy flow

Next we consider a benchmark inverse problem from subsurface flow modeling [21] and electrical impedance tomography [24]. Consider the PDE

$$\begin{aligned} -\nabla \cdot (a(s)\nabla p(s)) &= f(s) & s \in (0, 1)^2 \\ p(s) &= 0 & s \in \partial(0, 1)^2 \end{aligned} \quad (9)$$

We interpret $p(s)$ as the pressure field of subsurface flow in a reservoir with permeability coefficients $a(s)$ under the forcing $f(s)$. We further consider a two-scale model for the permeability field $a(s) = A\mathbb{1}_{\Omega_A}(s) + B\mathbb{1}_{\Omega_B}(s)$ where $\Omega_A, \Omega_B \subset [0, 1]^2$ are disjoint and such that $\Omega_A \cup \Omega_B = [0, 1]^2$, and model $A \sim U(3, 5)$ and $B \sim U(12, 16)$. Figure 4(a) shows the sets Ω_A (yellow) and Ω_B (blue) in our experiments. We consider the inverse problem of recovering the permeability parameters $\mathbf{y} = (A, B)$ from noisy measurements of the point values of the pressure field p , i.e., $\mathbf{x} = (p(s_1), \dots, p(s_{16})) + \gamma$, where $\gamma \sim N(0, 10^{-7}I_{16})$. Figure 4(b) shows an example of a pressure field along with the measurement locations s_j (red dots).

We train an MGAN using $N = 100000$ training points by sampling A, B and solving the PDE (9) using finite differences. We then test the MGAN conditional samples at new inputs \mathbf{x}_j^* for $j = 1, 2, 3$, generated by solving the PDE (9) with $(A, B) = (3.5, 13)$, $(4, 14)$, and $(4.5, 15)$, respectively; hence we expect $\mathbf{y}|\mathbf{x}_j^*$ to concentrate around these prescribed values. Figures 4(b)–(d) shows conditional KDEs computed with 30,000 MCMC samples while 4(f)–(h) shows conditional KDEs from 30,000 MGAN samples. Once again we observe that the MGAN map captures the conditional with good accuracy. For more results and details involving this example see Section E.3.

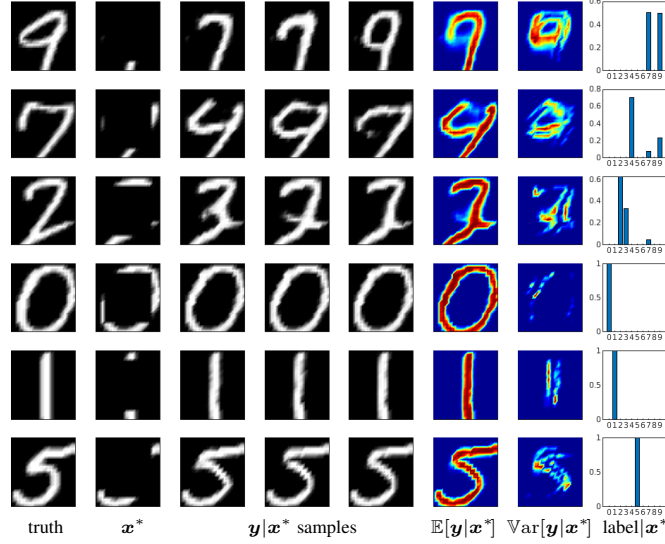


Figure 5: Example in-painted images using MGANs. The first column shows the ground truth images. The second column shows x^* the image to be in-painted. The third, fourth, and fifth columns show random in-paintings generated from the conditional $y|x^*$. The sixth and seventh columns show the pixel-wise conditional mean and variance computed from 1000 samples. The last column shows the label probabilities of samples from $y|x^*$ classified using LeNet [28].

3.4 Image in-painting

For our final set of experiments we consider the image in-painting problem, where an image is reconstructed after having some sections removed. We view this problem as an image-to-image regression problem where the input x is the incomplete image and the output y is the in-painting. We consider the full MNIST training dataset consisting of 20×20 images of handwritten digits, and as input x we remove the middle 14×14 pixels by setting their values to zero so $x \in \mathbb{R}^{20 \times 20}$ and output $y \in \mathbb{R}^{14 \times 14}$ is the removed pixels. While MNIST is usually considered too “simple” for modern machine learning applications, we choose this dataset as it allows us to use simple neural network architectures that do not require much tuning and, more importantly, to showcase the UQ benefits offered by MGANs.

We train an MGAN on the MNIST training set and for 800 randomly selected images x^* from the MNIST test set, generate 1000 possible in-paintings. We then compute the pixel-wise variances of these samples and rank them from least to most variable according to the L_2 -norm of variances. Figure 5 shows our in-painting results for the digits 9, 7, 2, 0, 1, 5. The first column of Figure 5 shows the original “truth” images from MNIST. The second column shows the incomplete images x^* while the third to fifth columns depict three representative samples from $\nu(dy|x^*)$. The images in the sixth column show the mean of $y|x^*$ along with variances shown in the seventh column. The conditional samples are then labeled by a pre-trained classifier (LeNet [28]) to obtain classification probabilities for the in-paintings reported in the eighth column of Figure 5. Interestingly, we observe that in most cases the labels with highest probabilities correspond to visual inspection of the means.

The digits 9 and 7 have the highest variance due to their similar shapes. This can be seen from the variance (Column 7) of the first two rows in Figure 5. The highest variance region is the bottom of the loop in 9 since leaving it blank results in a 7. In contrast, digits such as 0 and 1 have the lowest variances since they can only be completed in distinct manners and the conditional variances for these digits are primarily due to stylistic changes.

4 Conclusion

We presented MGANs, a model-agnostic method for conditional sampling of outputs given new inputs. We constructed this method by adding monotonicity and block-triangular constraints to standard

GANs. Idealized theoretical results along with numerical experiments elucidate the effectiveness and versatility of MGANs with applications in supervised learning and inverse problems. Our exposition suggests numerous future directions of research: The interplay between the quality of the full MGAN map obtained from (5) and the accuracy of the derived conditionals warrants future theoretical investigation. Relatedly, approximation results characterizing the expressiveness of block-triangular maps would be of interest. Extension of the MGANs to conditional sampling on infinite-dimensional function spaces is another exciting research direction, pertinent to inverse problems.

Statement of broader impact

This article focuses on novel mathematical techniques that enable model agnostic uncertainty quantification in supervised learning. To this end, this work brings together ideas from the fields of machine learning, inverse problems, and uncertainty quantification and connects these three communities consisting of computer scientists, mathematicians, and statisticians. Broadly speaking, uncertainty quantification offers crucial benefits in machine learning applications as it allows practitioners to quantify their confidence in predictions and to assess the amount of trust that can be put in algorithms. This is a crucial tool in many medical and societal applications as we continuously choose to put more trust in computer programs and software to perform complicated inference and classification tasks.

References

- [1] L. Ambrogioni, U. Güçlü, M. A. van Gerven, and E. Maris. The kernel mixture network: A nonparametric method for conditional density estimation of continuous random variables. *arXiv preprint:1705.07111*, 2017.
- [2] M. Arbel and A. Gretton. Kernel conditional exponential family. In *Proceedings of the Twenty-First International Conference on Artificial Intelligence and Statistics*, pages 1337–1346, 2018.
- [3] M. Arjovsky, S. Chintala, and L. Bottou. Wasserstein generative adversarial networks. In *ICML*, pages 214–223, 2017.
- [4] J. M. Bardsley, A. Solonen, H. Haario, and M. Laine. Randomize-then-optimize: A method for sampling from posterior distributions in nonlinear inverse problems. *SIAM Journal on Scientific Computing*, 36(4):A1895–A1910, 2014.
- [5] D. Bigoni, O. Zahm, A. Spantini, and Y. Marzouk. Greedy inference with layers of lazy maps. *arXiv preprint arXiv:1906.00031*, 2019.
- [6] C. M. Bishop. Mixture density networks. Technical Report NCRG/94/004, Aston University, Department of Computer Science and Applied Mathematics, 1994.
- [7] V. I. Bogachev. *Measure Theory*, volume 2. Springer, New York, 2007.
- [8] R. T. Q. Chen, J. Behrmann, D. K. Duvenaud, and J.-H. Jacobsen. Residual flows for invertible generative modeling. In *Advances in Neural Information Processing Systems 32*, pages 9916–9926. Curran Associates, Inc., 2019.
- [9] C. Doersch. Tutorial on variational autoencoders. *arXiv preprint arXiv:1606.05908*, 2016.
- [10] T. A. El Moselhy and Y. M. Marzouk. Bayesian inference with optimal maps. *Journal of Computational Physics*, 231(23):7815–7850, 2012.
- [11] C. W. Fox and S. J. Roberts. A tutorial on variational bayesian inference. *Artificial intelligence review*, 38(2):85–95, 2012.
- [12] A. Gelman, J. B. Carlin, H. S. Stern, D. B. Dunson, A. Vehtari, and D. B. Rubin. *Bayesian data analysis*. CRC press, 2013.
- [13] S. Ghosal, J. K. Ghosh, A. W. Van Der Vaart, et al. Convergence rates of posterior distributions. *Annals of Statistics*, 28(2):500–531, 2000.
- [14] E. Giné and R. Nickl. *Mathematical foundations of infinite-dimensional statistical models*, volume 40. Cambridge University Press, 2016.
- [15] I. Goodfellow, J. Pouget-Abadie, M. Mirza, B. Xu, D. Warde-Farley, S. Ozair, A. Courville, and Y. Bengio. Generative adversarial nets. In Z. Ghahramani, M. Welling, C. Cortes, N. D.

- Lawrence, and K. Q. Weinberger, editors, *Advances in Neural Information Processing Systems* 27, pages 2672–2680. Curran Associates, Inc., 2014.
- [16] A. Grelaud, C. P. Robert, J.-M. Marin, F. Rodolphe, J.-F. Taly, et al. Abc likelihood-free methods for model choice in gibbs random fields. *Bayesian Analysis*, 4(2):317–335, 2009.
 - [17] F. Gressmann, F. J. Király, B. Mateen, and H. Oberhauser. Probabilistic supervised learning. *arXiv preprint arXiv:1801.00753*, 2019.
 - [18] J. Gui, Z. Sun, Y. Wen, D. Tao, and J. Ye. A review on generative adversarial networks: Algorithms, theory, and applications. *arXiv preprint: 2001.06937*, 2020.
 - [19] M. U. Gutmann and J. Corander. Bayesian optimization for likelihood-free inference of simulator-based statistical models. *The Journal of Machine Learning Research*, 17(1):4256–4302, 2016.
 - [20] T. Hastie, R. Tibshirani, and J. Friedman. *The elements of statistical learning: data mining, inference, and prediction*. Springer Science & Business Media, 2009.
 - [21] M. A. Iglesias, K. Lin, and A. M. Stuart. Well-posed Bayesian geometric inverse problems arising in subsurface flow. *Inverse Problems*, 30(11):114001, 2014.
 - [22] P. Isola, J. Zhu, T. Zhou, and A. A. Efros. Image-to-image translation with conditional adversarial networks. *CoRR*, abs/1611.07004, 2016.
 - [23] S. I. Kabanikhin. *Inverse and Ill-posed Problems: Theory and Applications*, volume 55 of *Inverse and Ill-posed Problems*. De Gruyter, 2011.
 - [24] J. Kaipio and E. Somersalo. *Statistical and Computational Inverse Problems*, volume 160 of *Applied Mathematical Sciences*. Springer Science & Business Media, New York, 2005.
 - [25] D. P. Kingma and P. Dhariwal. Glow: Generative flow with invertible 1x1 convolutions. In *Advances in Neural Information Processing Systems 31*, pages 10215–10224. Curran Associates, Inc., 2018.
 - [26] D. P. Kingma, T. Salimans, R. Jozefowicz, X. Chen, I. Sutskever, and M. Welling. Improving Variational Inference with Inverse Autoregressive Flow. *CoRR*, abs/1606.04934, 2016.
 - [27] I. Kobyzev, S. Prince, and M. A. Brubaker. Normalizing flows: Introduction and ideas. *arXiv preprint arXiv:1908.09257*, 2019.
 - [28] Y. Lecun, L. Bottou, Y. Bengio, and P. Haffner. Gradient-based learning applied to document recognition. In *Proceedings of the IEEE*, pages 2278–2324, 1998.
 - [29] J. Lin. Divergence measures based on the shannon entropy. *IEEE Transactions on Information theory*, 37(1):145–151, 1991.
 - [30] Y. Marzouk, T. Moselhy, M. Parno, and A. Spantini. Sampling via measure transport: An introduction. *Handbook of Uncertainty Quantification*, pages 1–41, 2016.
 - [31] M. Mirza and S. Osindero. Conditional generative adversarial nets. *arXiv preprint arXiv:1411.1784*, 2014.
 - [32] S. Nowozin, B. Cseke, and R. Tomioka. f-gan: Training generative neural samplers using variational divergence minimization. In D. D. Lee, M. Sugiyama, U. V. Luxburg, I. Guyon, and R. Garnett, editors, *Advances in Neural Information Processing Systems* 29, pages 271–279. Curran Associates, Inc., 2016.
 - [33] G. Papamakarios and I. Murray. Fast ϵ -free inference of simulation models with bayesian conditional density estimation. In *Advances in Neural Information Processing Systems*, pages 1028–1036, 2016.
 - [34] G. Papamakarios, E. Nalisnick, D. J. Rezende, S. Mohamed, and B. Lakshminarayanan. Normalizing flows for probabilistic modeling and inference. *arXiv preprint arXiv:1912.02762*, 2019.
 - [35] G. Papamakarios, T. Pavlakou, and I. Murray. Masked autoregressive flow for density estimation. In *Advances in Neural Information Processing Systems* 30, pages 2338–2347. Curran Associates, Inc., 2017.
 - [36] G. Papamakarios, D. Sterratt, and I. Murray. Sequential neural likelihood: Fast likelihood-free inference with autoregressive flows. In *The 22nd International Conference on Artificial Intelligence and Statistics*, pages 837–848, 2019.

- [37] M. Parno and Y. Marzouk. Transport map accelerated Markov chain Monte Carlo. *arXiv preprint arXiv:1412.5492*, 2014.
- [38] M. D. Parno. *Transport maps for accelerated Bayesian computation*. PhD thesis, Massachusetts Institute of Technology, 2015.
- [39] A. Radford, L. Metz, and S. Chintala. Unsupervised representation learning with deep convolutional generative adversarial networks. *arXiv preprint:1511.06434*, 2015.
- [40] C. Robert and G. Casella. *Monte Carlo statistical methods*. Springer Science & Business Media, 2013.
- [41] J. Rothfuss, F. Ferreira, S. Walther, and M. Ulrich. Conditional density estimation with neural networks: Best practices and benchmarks. *arXiv preprint:1903.00954*, 2019.
- [42] F. Santambrogio. Optimal transport for applied mathematicians. *Birkäuser, NY*, 55:58–63, 2015.
- [43] M. Shiga, V. Tangkaratt, and M. Sugiyama. Direct conditional probability density estimation with sparse feature selection. *Machine Learning*, 100(2-3):161–182, 2015.
- [44] A. Spantini, R. Baptista, and Y. Marzouk. Coupling techniques for nonlinear ensemble filtering. *arXiv preprint arXiv:1907.00389*, 2019.
- [45] A. M. Stuart. Inverse problems: a Bayesian perspective. *Acta Numerica*, 19:451–559, 2010.
- [46] C. Villani. *Optimal transport: Old and new*, volume 338 of *Grundlehren der mathematischen Wissenschaften*. Springer, New York, 2009.
- [47] H. Yang and E. G. Tabak. Conditional density estimation, latent variable discovery and optimal transport. *arXiv preprint arXiv:1910.14090*, 2019.
- [48] E. Zeidler. *Nonlinear Functional Analysis and Its Applications: II/B: Nonlinear Monotone Operators*. Springer Science & Business Media, New York, 2013.
- [49] J.-Y. Zhu, R. Zhang, D. Pathak, T. Darrell, A. A. Efros, O. Wang, and E. Shechtman. Toward multimodal image-to-image translation. In *Advances in Neural Information Processing Systems 30*, pages 465–476. Curran Associates, Inc., 2017.

Appendix

Here we collect additional discussions, theoretical results, and numerical experiments that complement the manuscript titled “Conditional sampling with monotone GANs.” Section A expands upon the introductory remarks of Section 1 in the main article, discussing the connections between conditional sampling and supervised learning, and the potential benefits of uncertainty quantification (UQ). Section B summarizes the details of the MGAN training procedure along with a summary of the MGAN algorithm and complements Section 2.2 of the main article. Section C contains the proof of Theorem 1 in the article. Finally, Section E contains additional examples and details pertaining to the numerical results in the main article and in particular in Section 3.

A Discussion

Here we collect further discussions surrounding conditional sampling, MGANs, and other topics in statistics, machine learning, and applied mathematics. Subsection A.1 discusses the connections between conditional sampling and supervised learning (SL) as well as the importance of UQ for SL. In Subsection A.2, we present MGANs as a method for likelihood-free inference. In Subsection A.3 we outline applications of MGANs in the solution of inverse problems with black-box forward maps.

A.1 A model agnostic approach to SL and UQ

Conditional sampling can be viewed as the problem of generating samples from certain “slices” of a probability measure $\nu(d\mathbf{x}, d\mathbf{y})$. As demonstrated in the cartoon image in Figure 6 conditioning the output \mathbf{y} on a new point \mathbf{x}^* amounts to restricting $\nu(d\mathbf{x}, d\mathbf{y})$ along the hyperplane $\mathbf{x} = \mathbf{x}^*$, renormalizing this function and then generating samples from the resulting distribution.

As we briefly mentioned in Section 1, conditional sampling problems are ubiquitous in statistics, applied mathematics, and engineering. For example, most inference problems reduce to conditional

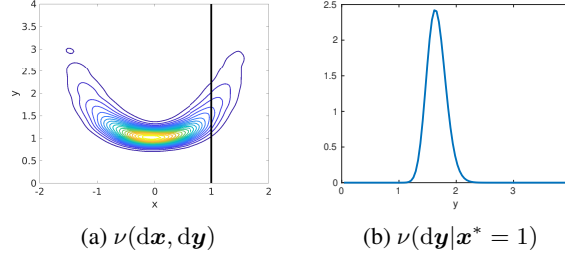


Figure 6: Schematic of conditional sampling. (a) The probability density function of the joint input and output measure $\nu(dx, dy)$ (b) The probability density function of the conditional measure $\nu(dy|x^* = 1)$ as a normalized slice of the joint measure.

sampling where one wishes to characterize an output parameter y at a new input parameter x^* . In regression, we often wish to estimate $y(x^*)$ for $x^* \in X \subset \mathbb{R}^n$, i.e., a certain subset of the input parameter space. As we also mentioned in Section 1, most SL algorithms such as ridge, LASSO, or neural network regression assume a functional relationship $y = G(x)$ and estimate G within certain parametric function spaces.

A core assumption at the heart of classic point estimation methods is the existence of a ground truth function G that could predict y at any new input x^* . If a good approximation \hat{G} to G can be computed, then one can predict the output y at the new input x^* simply by setting $y = \hat{G}(x^*)$. However, the estimate \hat{G} is dependent on the training data and the approximation power of the chosen parameterization in relation to the ground truth G .

With this issue in mind, it is natural to resort to a statistical model that characterizes \hat{G} as a random variable, leading to the statistical or probabilistic perspective on SL [20, 17]. Such probabilistic formulations, be they frequentist or Bayesian, have a major advantage over deterministic methods: the ability to characterize “uncertainties” in the predicted output $y|x^*$. Loosely speaking, the word “uncertainty” here refers to meaningful statistics of $y|x^*$ that characterize the variability of the predicted output, e.g., its mean and covariance. In the Bayesian setting, such statistics can be approximated using sampling methods such as MCMC [40], variational techniques [11], or in simpler cases, via closed-form conjugacy relationships [12]. In this regard, the MGANs approach introduced in the article belongs to the category of sampling techniques such as MCMC, whose goal is to generate independent samples from the law of $y|x^*$, as opposed to assuming some structural form of the probability measure directly.

However, a major advantage of MGANs (and also the triangular maps of [30]) is that the method is *model-agnostic*: the MGAN approach does not require prior knowledge of the form of G or any specific parameterization of \hat{G} . This is “in principle,” of course, and under the assumption that the neural networks used to describe the transport maps in MGANs are expressive enough to capture the ground truth transport maps pushing the reference η to the target ν . The synthetic example in Section 3.1 demonstrates this feature of MGANs clearly: the joint target ν as well as the conditionals $\nu(dy|x^*)$ are computed accurately for three different choices of G , but using the same architecture and training procedure within the MGAN approach. Differences among the three models in that example are due *only* to the training sets.

It is important to note that while model-agnostic approaches such as MGANs and triangular maps appear to be extremely flexible and general tools for inference, their theoretical properties—in particular the sample complexities needed to approximate the transport maps to a given accuracy—are largely open questions. A large body of theoretical research is dedicated to studying the consistency of classic statistical SL procedures from the Bayesian and frequentist perspectives, focusing on conditions and asymptotic regimes under which the estimated probability measure on $y|x^*$ or \hat{G} contracts around a certain “ground truth” at a certain rate depending on the size and quality of training data [13, 14]. To the best of our knowledge, such detailed analysis has not been performed for measure transport techniques such as MGANs.

A.2 MGANs and likelihood-free Bayesian inference

Due to model agnosticism and the fact that the training process relies only on samples from the joint distribution $\nu(d\mathbf{y}, d\mathbf{x})$, MGANs can be readily applied for likelihood-free inference [16, 19, 36, 33] and approximate Bayesian computation tasks, i.e., problems where the likelihood function is intractable or expensive to evaluate. Our numerical experiments in Subsections E.2 and 3.3 illustrate these applications, where evaluation of the likelihood may require the solution of a complicated ODE or PDE model. However, the training of MGANs does not require any likelihood evaluations or evaluations of the differential equations *during* training; once the training dataset is given, the MGAN can be trained independently. This makes the MGAN approach particularly attractive in applications where the input-to-output map involves an stochastic process, differential equation, PDE, or a black-box expensive computer model.

A.3 MGANs and Bayesian inverse problems

One specific application area for MGANs in the context of likelihood-free inference is inverse problems [23, 45]. Broadly speaking, inverse problems can be viewed as SL algorithms where the input and output parameters belong to high or possibly infinite-dimensional Banach spaces. More precisely, a prototypical inverse problem takes the form

$$\mathcal{L}(\mathbf{y})\mathbf{u} = 0, \quad \mathbf{x} = g(\mathbf{u}), \quad (10)$$

where $(\mathbf{x}, \mathbf{y}, \mathbf{u}) \in X \times Y \times U$ with Banach spaces X, Y, U . For any fixed \mathbf{y} , $\mathcal{L}(\mathbf{y})$ is a known map which is assumed to be invertible, although the inverse map need not have a closed form expression; in the Darcy flow example \mathcal{L} is a differential operator. The function $g : U \rightarrow X$ is the observation map that extracts the “measurements” \mathbf{x} from \mathbf{u} ; in the Darcy flow example this map is given by the pointwise evaluation function on the pressure field. Then, solving the inverse problem refers to estimation of \mathbf{y} given a fixed observation \mathbf{x}^* possibly polluted by some noise. The main challenge in solution of inverse problems is *ill-posedness*, i.e., the mapping from $\mathbf{y} \mapsto \mathbf{x}$ is not stably invertible. Hence, regularization is needed. Note that our notation is at odds with the standard notation in statistics and inverse problems where \mathbf{y} often denotes the data and \mathbf{x} often denotes the input parameters. We choose this idiosyncratic notation to remain consistent with machine learning notation where \mathbf{x} denotes the input data and \mathbf{y} denotes the output to be estimated.

A popular method for regularization of inverse problems, and in turn their solution, is to employ Bayes’ rule [45] by imposing a prior on \mathbf{y} along with a likelihood function extracted from (10) leading to a posterior measure on $\nu(d\mathbf{y}|\mathbf{x}^*)$. However, since the spaces X, Y are possibly high or infinite-dimensional and the forward map $\mathbf{y} \mapsto \mathbf{x}$ is often nonlinear, it is usually not possible to characterize $\nu(d\mathbf{y}|\mathbf{x}^*)$ analytically. Thus, sampling techniques such as MCMC are employed to estimate moments and other attributes of the posterior measure, and in turn to characterize the true value of \mathbf{y} given \mathbf{x}^* and its uncertainty.

In high dimensions, methods such as Metropolis-Hastings require us to solve (10) many times to evaluate likelihood functions as part of the accept/reject step, which can be computationally demanding. This is the juncture where MGANs, and similarly the triangular maps of [30], offer an interesting alternative for sampling Bayesian posteriors. One can proceed to generate a fixed number of samples from the prior on \mathbf{y} , say $\mathbf{y}_1, \dots, \mathbf{y}_N$ and solve (10) to obtain measurements $\mathbf{x}_1, \dots, \mathbf{x}_N$. The pairs $\{\mathbf{x}_j, \mathbf{y}_j\}_{j=1}^N$ can now be used as training data within the MGANs procedure to obtain a transport map that can push the reference $\eta(d\mathbf{y})$ to the Bayesian posterior $\nu(d\mathbf{y}|\mathbf{x}^*)$ at the new observed data \mathbf{x}^* . Note that we readily employed this approach in the “with prior” BOD example in Subsection E.2. While the works [30, 5, 10, 44] explore the use of triangular maps for solving inverse problems, it is interesting to study possible improvements and contributions of the MGANs procedure in this direction.

B The MGAN training procedure

Here we present further details on the MGAN training procedure, leading to Algorithm 1 for training MGANs and used in our numerical experiments.

Recall the measure transport problem (2) with the divergence D replaced with the GAN functional [32]

$$\begin{aligned} & \min_{\mathsf{T}} \sup_{f \in \mathcal{F}} \mathbb{E}_{\mathbf{z} \sim \nu} [\log f(\mathbf{z})] + \mathbb{E}_{\mathbf{w} \sim \eta} [\log(1 - f(\mathsf{T}(\mathbf{w})))] , \\ & \text{subject to } \langle \mathsf{T}(\mathbf{w}) - \mathsf{T}(\mathbf{w}'), \mathbf{w} - \mathbf{w}' \rangle > 0, \quad \forall \mathbf{w}, \mathbf{w}' \in \text{supp } \eta, \\ & \mathsf{T}(\mathbf{x}, \mathbf{y}) = \begin{bmatrix} \mathsf{K}(\mathbf{x}) \\ \mathsf{F}(\mathsf{K}(\mathbf{x}), \mathbf{y}) \end{bmatrix}, \end{aligned}$$

where we have explicitly outlined the parameterization and constraints imposed on T . The function class \mathcal{F} is currently arbitrary and denotes the space of discriminators; for example one can choose $\mathcal{F} = C(\mathbb{R}^d; (0, 1))$, the space of continuous on \mathbb{R}^d taking values in $(0, 1)$. We now approximate this optimization problem in three stages.

First, let $\widehat{\mathsf{K}}(\cdot; \boldsymbol{\alpha}) : \mathbb{R}^n \rightarrow \mathbb{R}^n$ and $\widehat{\mathsf{F}}(\cdot; \boldsymbol{\beta}) : \mathbb{R}^d \rightarrow \mathbb{R}^m$ be neural networks that approximate the components K, F of the map T , with $\boldsymbol{\alpha}, \boldsymbol{\beta}$ denoting the parameters of these networks. Letting $\boldsymbol{\theta} := (\boldsymbol{\alpha}, \boldsymbol{\beta})$ denote the collection of all of the parameters in $\widehat{\mathsf{K}}, \widehat{\mathsf{F}}$ we define the neural network $\widehat{\mathsf{T}}(\cdot; \boldsymbol{\theta}) : \mathbb{R}^d \rightarrow \mathbb{R}^d$ that approximates T :

$$\widehat{\mathsf{T}}(\mathbf{x}, \mathbf{y}; \boldsymbol{\theta}) = \begin{bmatrix} \widehat{\mathsf{K}}(\mathbf{x}; \boldsymbol{\alpha}) \\ \widehat{\mathsf{F}}(\widehat{\mathsf{K}}(\mathbf{x}; \boldsymbol{\alpha}), \mathbf{y}; \boldsymbol{\beta}) \end{bmatrix}. \quad (11)$$

Moreover, we parameterize f as a neural network with weights $\boldsymbol{\theta}'$, thereby taking \mathcal{F} to be the space of functions spanned by the discriminator network architecture for admissible choices of the weights $\boldsymbol{\theta}'$, respecting the constraint that $f(\cdot; \boldsymbol{\theta}')$ take values in $(0, 1)$.

Next, we relax the strict monotonicity constraint on T by replacing it with an average monotonicity condition on $\widehat{\mathsf{T}}$. More precisely, we require

$$\mathbb{E}_{\mathbf{z} \sim \eta} \mathbb{E}_{\mathbf{z}' \sim \eta} \langle \widehat{\mathsf{T}}(\mathbf{z}; \boldsymbol{\theta}) - \widehat{\mathsf{T}}(\mathbf{z}'; \boldsymbol{\theta}), \mathbf{z} - \mathbf{z}' \rangle > 0. \quad (12)$$

While this condition does not ensure that $\widehat{\mathsf{T}}$ is monotone everywhere (or at least on the support of η), numerically we find that it is sufficient to ensure that $\widehat{\mathsf{T}}$ is monotone with high probability. In particular, we compute a numerical approximation of

$$\mathbb{P}_{\mathbf{z}, \mathbf{z}' \sim \eta} [\langle \widehat{\mathsf{T}}(\mathbf{z}; \boldsymbol{\theta}) - \widehat{\mathsf{T}}(\mathbf{z}'; \boldsymbol{\theta}), \mathbf{z} - \mathbf{z}' \rangle > 0]. \quad (13)$$

The monotonicity probability can be approximated during the training procedure as shown in Table 3. We find that tracking this probability is helpful during training as it reveals how $\widehat{\mathsf{T}}$ satisfies the sufficient constraints for the existence of the push-forward conditional measure.

In the third and final stage of approximation, we replace the expectations in B with empirical averages over training data and mini-batch samples from the reference η as in the standard GAN training procedure [15]. We outline the resulting approach in Algorithm 1, which was used in our numerical experiments in Section 3. Following [15], we train $\widehat{\mathsf{T}}$ to maximize $\log f(\widehat{\mathsf{T}}(\mathbf{w}))$ instead of minimizing $\log(1 - f(\widehat{\mathsf{T}}(\mathbf{w})))$. For fully-connected networks, we use the RMSProp optimizer,

and for convolutional networks, we use Adam. Hyperparameters are given in Section E for each numerical experiment.

Algorithm 1: Outline of the MGAN training procedure.

Data: Training set $\{\mathbf{x}_j, \mathbf{y}_j\}_{j=1}^M \stackrel{i.i.d.}{\sim} \nu(\mathrm{d}\mathbf{x}, \mathrm{d}\mathbf{y})$.

Input: Generator $\hat{\mathbf{T}}(\mathbf{x}, \mathbf{y}; \boldsymbol{\theta}) = (\hat{\mathbf{K}}(\mathbf{x}; \boldsymbol{\alpha}), \hat{\mathbf{F}}(\hat{\mathbf{K}}(\mathbf{x}, \boldsymbol{\alpha}), \mathbf{y}; \boldsymbol{\beta}))$ with parameters $\boldsymbol{\theta} = (\boldsymbol{\alpha}, \boldsymbol{\beta})$, discriminator $f(\mathbf{x}, \mathbf{y}; \boldsymbol{\theta}')$ with parameters $\boldsymbol{\theta}'$, monotonicity penalty parameter $\lambda > 0$.

Result: Mapping $\hat{\mathbf{F}}(\mathbf{x}, \mathbf{y}; \boldsymbol{\beta})$ satisfying $\hat{\mathbf{F}}(\mathbf{x}^*, \cdot; \boldsymbol{\beta})_{\#} \eta(\mathrm{d}\mathbf{y}) \approx \nu(\mathrm{d}\mathbf{y} | \mathbf{x}^*)$ for any $\mathbf{x}^* \sim \nu(\mathrm{d}\mathbf{x})$.

for number of training iterations **do**

 Generate 2ℓ reference samples $(\tilde{\mathbf{x}}_1, \tilde{\mathbf{y}}_1), \dots, (\tilde{\mathbf{x}}_{2\ell}, \tilde{\mathbf{y}}_{2\ell}) \stackrel{i.i.d.}{\sim} \eta$;

 Update $\hat{\mathbf{T}}$ by descending

$$\begin{aligned} \nabla_{\boldsymbol{\theta}} - \frac{1}{\ell} \sum_{j=1}^{\ell} \left[\log f(\hat{\mathbf{T}}(\tilde{\mathbf{x}}_j, \tilde{\mathbf{y}}_j; \boldsymbol{\theta})) \right. \\ \left. + \lambda \langle \hat{\mathbf{T}}(\tilde{\mathbf{x}}_j, \tilde{\mathbf{y}}_j; \boldsymbol{\theta}) - \hat{\mathbf{T}}(\tilde{\mathbf{x}}_{\ell+j}, \tilde{\mathbf{y}}_{\ell+j}; \boldsymbol{\theta}), (\tilde{\mathbf{x}}_j, \tilde{\mathbf{y}}_j) - (\tilde{\mathbf{x}}_{\ell+j}, \tilde{\mathbf{y}}_{\ell+j}) \rangle \right] \end{aligned}$$

 Sample minibatch of ℓ data points $(\mathbf{x}_{k_1}, \mathbf{y}_{k_1}), \dots, (\mathbf{x}_{k_\ell}, \mathbf{y}_{k_\ell})$ from training set;

 Update f by descending

$$\nabla_{\boldsymbol{\theta}'} - \frac{1}{\ell} \sum_{j=1}^{\ell} \left[\log f(\mathbf{x}_{k_j}, \mathbf{y}_{k_j}; \boldsymbol{\theta}') + \log \left(1 - f(\hat{\mathbf{T}}(\mathbf{z}_j^{\mathbf{x}}, \mathbf{z}_j^{\mathbf{y}}; \boldsymbol{\theta}); \boldsymbol{\theta}') \right) \right]$$

C Proof of Theorem 1

Here we present a simple proof of Theorem 1 following the proof of [30, Lem. 1]. First, let us introduce some notation. For $\mathbf{u} \in \mathbb{R}^m$ and $\mathbf{w} \in \mathbb{R}^n$ we let $\pi_{\eta}(\mathbf{u} | \mathbf{w})$ denote the Lebesgue density of $\eta(\mathrm{d}\mathbf{u} | \mathbf{w}^*)$, while $\pi_{\eta}(\mathbf{w}, \mathbf{u})$ denotes the Lebesgue density of $\eta(\mathrm{d}\mathbf{w}, \mathrm{d}\mathbf{u})$. Finally, $\pi_{\eta}(\mathbf{w})$ denotes the Lebesgue density of the marginal $\eta(\mathrm{d}\mathbf{w})$.

Fix $\mathbf{x}^* \in \mathbb{R}^n$ as the new input and let $\mathbf{w}^* := \mathbf{K}^{-1}(\mathbf{x}^*)$, which is well-defined since \mathbf{K} is surjective provided that \mathbf{T} is surjective. Now by the change of variables formula we have

$$\begin{aligned} \tilde{\mathbf{F}}(\mathbf{w}^*, \cdot)_{\#} \pi_{\eta}(\mathbf{y}) &= \pi_{\eta}(\tilde{\mathbf{F}}^{-1}(\mathbf{w}^*, \mathbf{y}) | \mathbf{w} = \mathbf{w}^*) |\det \nabla_{\mathbf{y}} \tilde{\mathbf{F}}^{-1}(\mathbf{w}^*, \mathbf{y})|, \\ &= \frac{\pi_{\eta}(\mathbf{w}^*, \tilde{\mathbf{F}}^{-1}(\mathbf{w}^*, \mathbf{y}))}{\pi_{\eta}(\mathbf{w}^*)} |\det \nabla_{\mathbf{y}} \tilde{\mathbf{F}}^{-1}(\mathbf{w}^*, \mathbf{y})|, \\ &= \frac{\pi_{\eta}(\mathbf{w}^*, \tilde{\mathbf{F}}^{-1}(\mathbf{w}^*, \mathbf{y}))}{\pi_{\eta}(\mathbf{K}^{-1}(\mathbf{x}^*))} |\det \nabla_{\mathbf{y}} \tilde{\mathbf{F}}^{-1}(\mathbf{w}^*, \mathbf{y})|. \end{aligned}$$

Another application of the change of variables formula to the denominator then yields

$$\tilde{\mathbf{F}}(\mathbf{w}^*, \cdot)_{\#} \pi_{\eta}(\mathbf{y}) = \frac{\pi_{\eta}(\mathbf{K}^{-1}(\mathbf{x}^*), \tilde{\mathbf{F}}^{-1}(\mathbf{K}^{-1}(\mathbf{x}^*), \mathbf{y}))}{\pi_{\nu}(\mathbf{x}^*)} |\det \nabla_{\mathbf{x}} \mathbf{K}^{-1}(\mathbf{x}^*)| |\det \nabla_{\mathbf{y}} \tilde{\mathbf{F}}^{-1}(\mathbf{K}^{-1}(\mathbf{x}^*), \mathbf{y})|,$$

where $\pi_{\nu}(\mathbf{x}^*)$ is the Lebesgue density of the marginal $\nu(\mathrm{d}\mathbf{x})$ evaluated at \mathbf{x}^* . Using the change of variables formula once more we realize that the numerator is the Lebesgue density of $\mathbf{T}_{\#} \eta(\mathrm{d}\mathbf{x}, \mathrm{d}\mathbf{y}) = \nu(\mathrm{d}\mathbf{x}, \mathrm{d}\mathbf{y})$ and so by the definition of the conditional density we have

$$\tilde{\mathbf{F}}(\mathbf{w}^*, \cdot)_{\#} \pi_{\eta}(\mathbf{y}) = \frac{\pi_{\nu}(\mathbf{x}^*, \mathbf{y})}{\pi_{\nu}(\mathbf{x}^*)} = \pi_{\nu}(\mathbf{y} | \mathbf{x}^*).$$

D Non-existence of certain transport maps

In this section we consider a simple example where the reference η is supported on a lower dimensional space compared to the target ν and show that in this setting there cannot exist a transport map

pushing η to ν . Let $\eta = N(0, 1)$ and $\nu = N(0, I_2)$ and suppose that there exists a continuous map $T : \mathbb{R} \rightarrow \mathbb{R}^2$ such that $T_\# \eta = \nu$. Without loss of generality, we may express T as

$$T(x) = \begin{bmatrix} T^{(1)}(x) \\ T^{(2)}(x) \end{bmatrix}$$

for some $T^{(1)}, T^{(2)} \in C(\mathbb{R}; \mathbb{R})$. Let $\nu_1 = N(0, 1)$, $\nu_2 = N(0, 1)$ denote the two marginals of ν . Since, by assumption, $T_\# \eta = \nu$, we must have that $T_\#^{(1)} \eta = \nu_1$. Therefore, by continuity, $T^{(1)}(x) = \pm x$. By definition of a marginal, ν_2 is independent of $T^{(1)}(x)$ since it is integrated out. However $T^{(2)}$ depends solely on $x = \pm T^{(1)}(x)$ therefore ν_2 has constant density which is a contradiction of the fact that, by construction, $\nu_2 = N(0, 1)$.

Note that the above can be generalized to include discontinuous maps. We show it in the continuous case only for simplicity, as there can exist an infinite number of discontinuous maps T with the property that $T_\# N(0, 1) = N(0, 1)$, which complicates the proof. The choice of the Gaussian is also innocuous. We could have chosen any atomless measure η and set $\nu = \eta \otimes \eta$. In general, even when the target distribution is not a product of one-dimensional marginals, i.e., it has correlations, we still cannot guarantee existence of a transport map as we will always need “more noise” than the reference distribution can provide.

The goal of this simple example is to demonstrate that, in general, we cannot expect the existence of maps pushing low dimensional measures to high dimensional ones. Therefore, GANs and VAEs that employ low-dimensional latent spaces are not well suited for generic SL tasks unless we assume the data lie on a low dimensional manifold. This assumption is hard to check in practice and it becomes unclear how to create consistent algorithms without knowledge of the manifold geometry. We do note, however, that the massive empirical success of GANs and VAEs for image generation indicates that the manifold hypothesis, or some approximation of it, likely holds in imaging tasks.

E Details on the numerical experiments

In this section we give further details regarding the numerical experiments presented in the main article, including the architectures and hyperparameter choices during training. The extra details are presented in the same order as in Section 3, with the addition of Subsection E.5 where we discuss the average monotonicity constraints and their level of violation within the experiments.

E.1 A synthetic example

Since this example is two-dimensional, our parameterization (11) is automatically triangular and so we expect \hat{T} to approximate the KR map as it is a global minimizer of (2); further constraints can ensure that the KR map is indeed the unique minimizer [30]. Figure 7 shows the true KR map as well as our transport map \hat{T} for each of the three problems. Interestingly, we observe that the MGAN approximates the true KR map in all three cases.

Throughout these experiments we used the following hyperparameters and architectures to construct \hat{T} : For \hat{K} we use a fully-connected network with three hidden layers with (100, 200, 100) units, the Leaky ReLU nonlinearity, batch normalization, and no output nonlinearity. For \hat{F} , we use a fully-connected network with three hidden layers with (200, 500, 100) units, the Leaky ReLU nonlinearity, batch normalization, and no output nonlinearity. The discriminator f has the same architecture as \hat{F} , but without batch normalization, and a sigmoid output nonlinearity. We use RMSProp with a learning rate of 10^{-6} , weight decay of 10^{-4} , a batch size of 64, a monotonicity parameter $\lambda = 0.01$, and train for 1000 epochs.

E.2 Biochemical oxygen demand model

Following our discussion in Subsections A.2 and A.3 we note that the BOD problem as presented in Section E.2 is an instance of likelihood-free Bayesian inference problem. Indeed the state variable $B(t)$ is the solution to an ODE with model parameters $\mathbf{y} = (A, B)$. The input \mathbf{x} is then chosen as noisy observations of the state \mathcal{B} at certain time steps. Thus, in the language of inverse problems, the

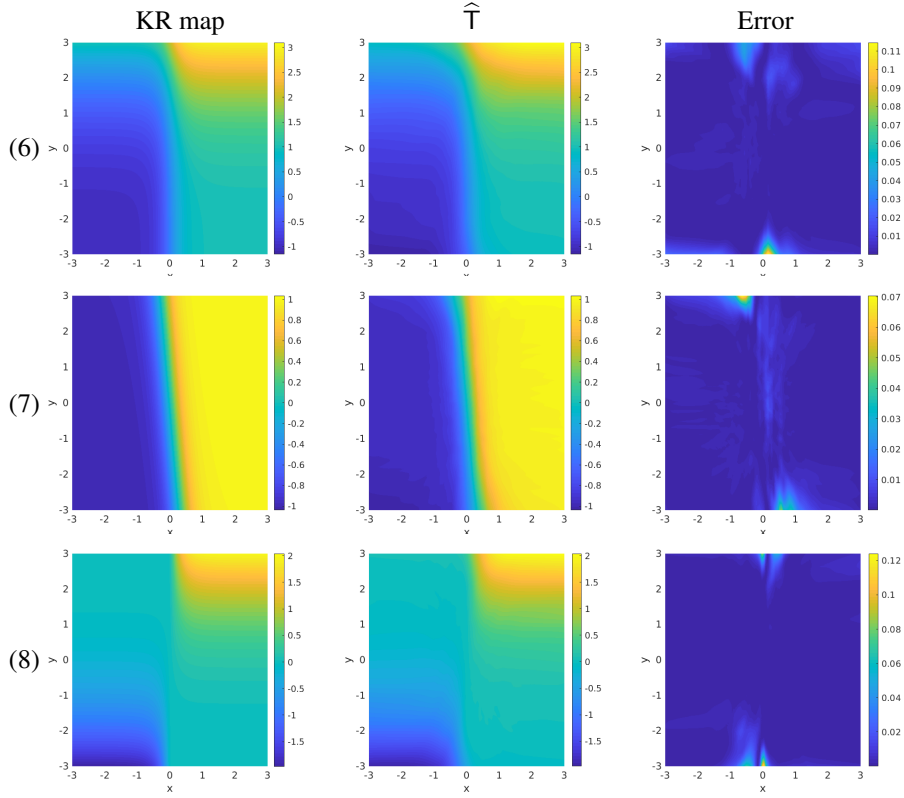


Figure 7: Each row corresponds to the problems (6),(7),(8) respectively. The first column shows the true KR map on $[-3, 3]^2$, the second column shows our transport map \hat{T} , and the last columns shows the absolute error between them.

MGAN sampling procedure amounts to sampling the posterior distribution of the unknown model parameters (A, B) conditioned on limited observations of the state $\mathcal{B}(t)$.

A standard Bayesian procedure might require formulating a likelihood function of the form

$$\Phi(\mathbf{x}; \mathbf{y}) = (5 \times 10^2) \sum_{j=1}^5 |x_j - \mathcal{B}(j; \mathbf{y})|^2,$$

where we used the notation $\mathcal{B}(j; \mathbf{y})$ to highlight the dependence of \mathcal{B} on the parameters (A, B) . Then a prior $\pi_0(\mathbf{y})$ should be chosen for the unknown parameters, yielding a posterior measure of the form

$$\pi_\nu(\mathbf{y}|\mathbf{x}^*) \propto \exp(-\Phi(\mathbf{x}^*; \mathbf{y}))\pi_0(\mathbf{y}).$$

The “without prior” approach in Section amounts to choosing $\pi_0 = U(0.4, 1.2) \otimes U(0.01, 0.31)$. However, the main difference between MGANs and standard sampling techniques such as MCMC is that MGANs does not require explicit evaluation of the likelihood function Φ . In the MGAN procedure we simply sample $\mathbf{y}_j \sim \pi_0$, and compute \mathbf{x}_j by solving the ODE with \mathbf{y}_j as the input and adding simulated observational noise to the outputs \mathbf{x}_j to construct the training set, the size of which will be limited by our computational budget. Once the training set is available the training of MGANs and the subsequent sampling of the posterior is done independently of the likelihood function or the ODE model.

The hyperparameter and architecture choices for this example are as follows. For \hat{K} we use a fully-connected network with three hidden layers with (256, 512, 128) units, the Leaky ReLU nonlinearity, batch normalization, and no output nonlinearity. We use the same architecture for \hat{F} and f , but the discriminator has no batch normalization, and a sigmoid output nonlinearity. We use RMSProp with a learning rate of 10^{-6} , weight decay of 10^{-4} , a batch size of 64, a monotonicity parameter $\lambda = 0.01$, and train for 1500 epochs.

E.3 Darcy flow

The Darcy flow example of Subsection 3.3 is another example of the likelihood-free solution of Bayesian inverse problems. The main difference between this example and the BOD example above is the that the input-output map involves the solution of an elliptic PDE. From the likelihood-free inference viewpoint, however, this modification has little effect on the MGAN training procedure beyond generation of the training data. In fact, MGANs can readily be applied to the solution of Bayesian inverse problems with black-box forward maps.

We now present complimentary numerical results for the Darcy flow problem. Table 2 shows further conditional statistics for the three test problems for various number of training points in comparison to statistics computed with MCMC as a benchmark. We observe that even with the smallest training set (size $N = 5000$), the mean and variance statistics are within acceptable range of the MCMC. While larger sample sizes help in most cases we observe a few outliers, especially in the skewness, where even with $N = 100000$ the MGAN estimates are quite different from MCMC.

Figure 8 shows further kernel density estimates of the conditional measures approximated from MGANs samples versus MCMC samples for different training set sizes. As expected, the quality of the MGAN sample KDE approximation improves as N increases. Another interesting feature is the fact that in the $N = 100000$ case with ground truth x_1^* , the MGAN KDE detects a hard constraint that is imposed by uniform prior. Note that this constraint appears sharply in the MCMC KDE since it is *explicitly* enforced within the MCMC procedure; however, this constraint is not explicitly implemented in the MGAN. We see that the constraint is not captured very well in the x_3^* case.

The choices of architectures and hyperparameters for the Darcy flow example are as follows. We used the *same* setting as in Section E.2 with the difference that \hat{F} and f have a linear layer at the beginning, mapping input $y \in \mathbb{R}^2$ to \mathbb{R}^{16} . This makes $\hat{K}(x; \alpha)$ and y have the same dimension.

Map type	$y x^*$	Mean		Variance		Skewness		Kurtosis	
		A	B	A	B	A	B	A	B
MCMC	$y x_1^*$	3.531	12.507	.0103	.1124	-.0050	.6674	2.900	3.111
	$y x_2^*$	3.748	14.555	.0159	.2565	.2337	-.0135	2.968	2.709
	$y x_3^*$	4.792	14.059	.0191	.2715	-.6581	.3269	2.970	3.097
MGAN $N = 100000$	$y x_1^*$	3.559	12.580	.0109	.1384	-.2394	.7353	3.130	3.282
	$y x_2^*$	3.752	14.538	.0170	.2557	.0263	-.0256	2.702	2.695
	$y x_3^*$	4.772	14.086	.0216	.3436	-.4702	.1279	2.972	2.782
MGAN $N = 50000$	$y x_1^*$	3.533	12.531	.0102	.1001	.0484	.5205	3.072	3.604
	$y x_2^*$	3.757	14.562	.0135	.2952	.1272	-.0042	3.267	2.921
	$y x_3^*$	4.784	14.048	.0153	.2991	-.7730	.4476	3.963	3.134
MGAN $N = 5000$	$y x_1^*$	3.593	12.534	.0058	.1394	-.0970	.0599	4.400	2.789
	$y x_2^*$	3.738	14.617	.0126	.1863	.0745	-.4216	3.044	3.056
	$y x_3^*$	4.794	14.053	.0193	.2857	.0173	.0188	3.147	2.789

Table 2: Statistics of $y|x^*$ for the Darcy flow problem.

E.4 Image in-painting

In this section we present the details of the in-painting experiments of Section 3.4. along with Figure 9 which presents examples of in-painting samples along with uncertainty estimates for all digits. We bias the presented results towards images with higher variance, i.e., where more than one posterior label is likely to appear.

We follow the convolutional architectures used in [39]. We first train \hat{K} as a standard GAN with the monotonicity constraint, setting $\lambda = 0.01$, i.e. we only update the parameters α . The map mimics the distribution of 20×20 MNIST images with their middle 14×14 section set to zero. We then train \hat{F} , holding α fixed, following Algorithm 1 again with $\lambda = 0.01$. \hat{F} has the same architecture as \hat{K} with the exception of a single hidden layer (1000 units) fully connected network at the beginning using a Leaky ReLU and smaller up-sampling scale factors to ensure the output is 14×14 . We take the output from $\hat{F} \circ \hat{K}$ and paste it into the middle 14×14 section of the output from \hat{K} to generate

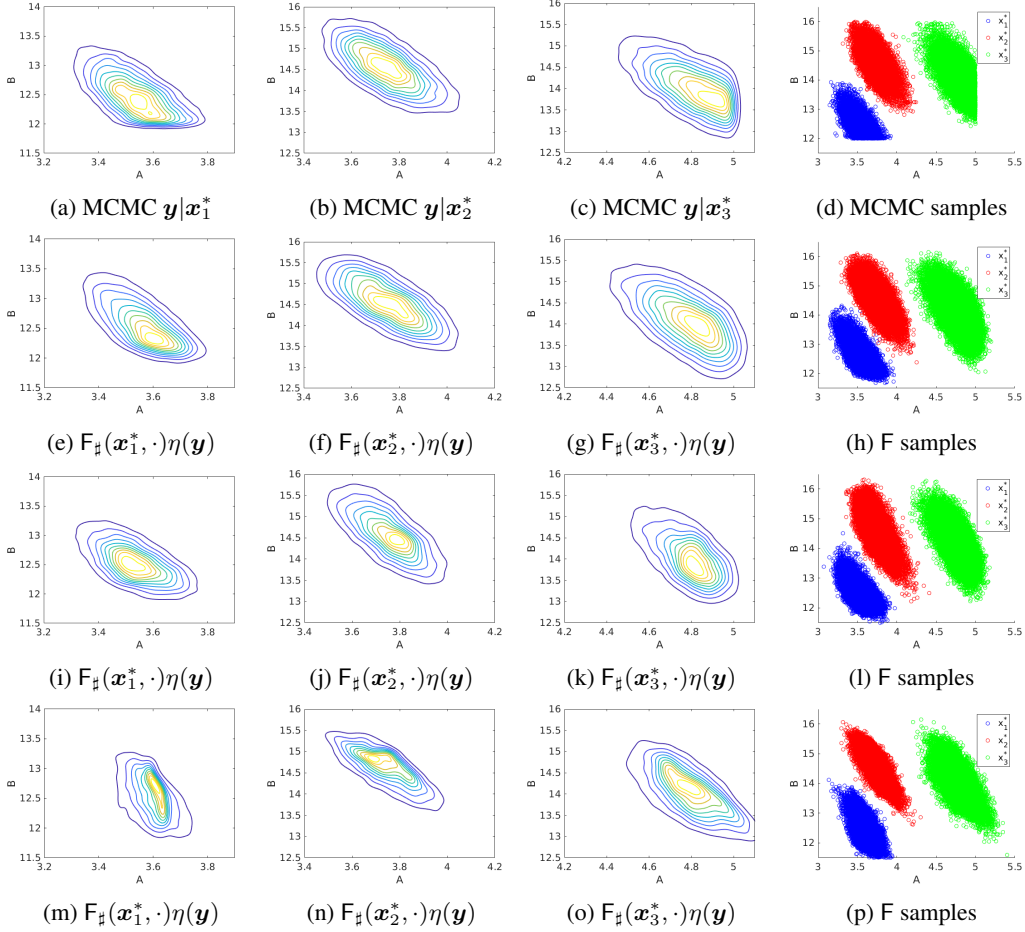


Figure 8: KDEs of the conditionals $y|x_j^*$ for the Darcy flow problem with $j = 1, 2, 3$. Each density is obtained by using 30,000 representative samples shown in the last column. The first row represents the ground truth obtained by MCMC. Each subsequent row shows the MGAN results when training with $N = 100000$, $N = 50000$, and $N = 5000$ data samples respectively.

images from the joint distribution. The discriminator follows the same architecture as in [39]. In both training procedures, we use the Adam optimizer with a learning of 2×10^{-4} , $\beta_1 = 0.5$, $\beta_2 = 0.999$, no weight decay, multiply the learning rate by 0.1 at the 100th, 300th, and 480th epoch, and train for a total of 500 epochs.

E.5 Average monotonicity violations

Our final set of results pertains to all of the numerical experiments above. Table 3 summarizes an approximation to the monotonicity probabilities of the trained MGANs in each experiment computed over samples from the reference. These probabilities were tracked during training using the mini-batch samples and averaged at each epoch. Here we report only the estimates computed at the final epoch as they constitute the approximate monotonicity probability of the trained model. We observe that even though the monotonicity constraint is only imposed in expectation, it still holds with high probability for the trained MGAN. The BOD experiment with prior has the lowest monotonicity probability at 89.36% while the Darcy flow example has the highest probability at 100%.

Further theoretical and numerical analysis of this expected monotonicity constraint is needed to better understand the reason for this good performance of the trained maps and also to understand the regularizing effects of this constraint in providing stability to the trained neural networks.

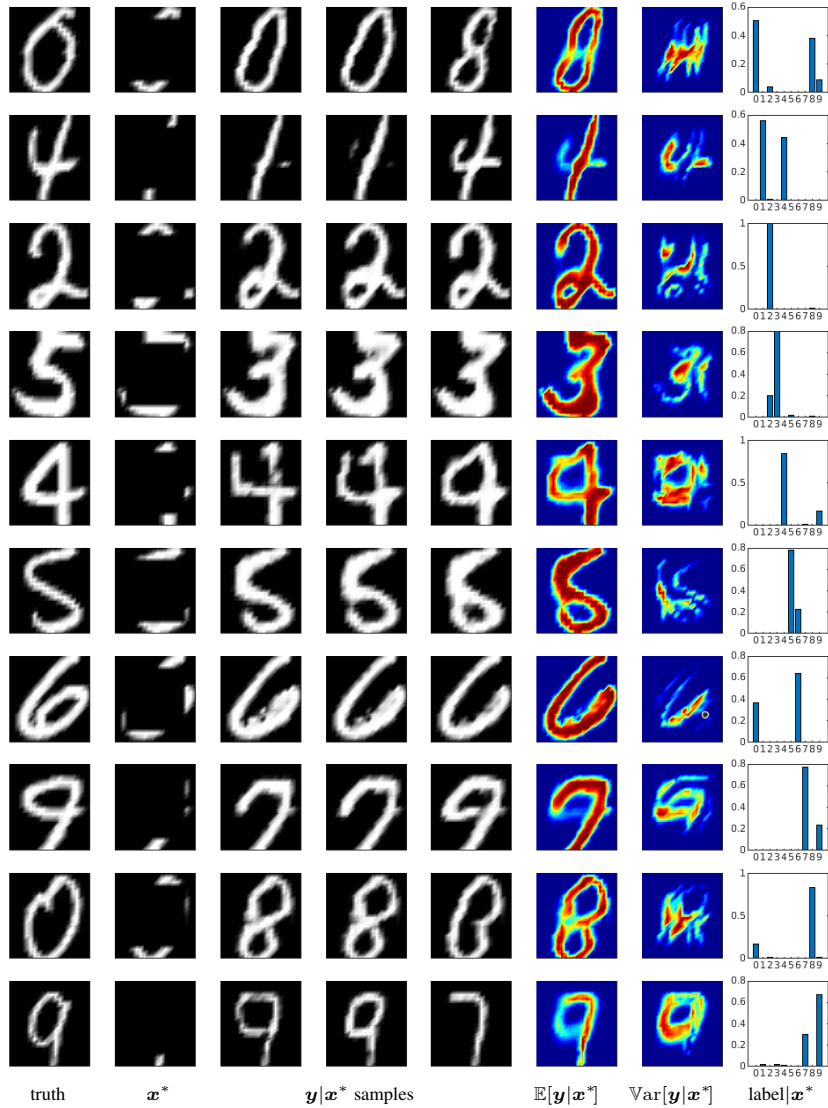


Figure 9: Example in-painted images using MGANs. The first column shows the ground truth images. The second column shows x^* the image to be in-painted. The third, fourth, and fifth columns show random in-paintings generated from the conditional $y|x^*$. The sixth and seventh columns show the pixel-wise conditional mean and variance computed from 1000 samples. The last column shows the label probabilities of samples from $y|x^*$ classified using LeNet [28].

	(6)	(7)	(8)	BOD (prior)	BOD (no prior)	Darcy	MNIST
Monotonicity	95.83%	92.71%	98.60%	89.36%	99.91%	100.0%	94.60%

Table 3: Final approximate probability that \hat{T} is monotone for each problem.